Chemical Engineering Journal 506 (2025) 160377

Contents lists available at ScienceDirect

Chemical Engineering Journal

journal homepage: www.elsevier.com/locate/cej

Ni-exsolved catalysts from hard templated mesoporous $LaNiO_3$ perovskite for highly efficient NH_3 decomposition

Sebastian Gamez [a,*], Ferdaous Ben Romdhane [b], Josefine Schnee [c], Eric M. Gaigneaux [a]

[a] Université catholique de Louvain (UCLouvain), Institute of Condensed Matter and Nanosciences (IMCN), Place Louis Pasteur 1. L04.01.09 1348 Louvain-la-Neuve, Belgium
[b] Sorbonne Université, Fédération de Chimie et Matériaux de Paris-Centre (FCMat), CNRS, Campus Pierre et Marie Curie, 4 Place Jussieu, F-75005 Paris Cedex 05 France
[c] Sorbonne Université, Laboratoire de Réactivité de Surface (LRS), CNRS, Campus Pierre et Marie Curie, 4 Place Jussieu, F-75005 Paris Cedex 05 France

ARTICLE INFO

Keywords:
Perovskite
Ammonia decomposition
Ammonia cracking
Hydrogen
Exsolution
Nickel
Hard templating

ABSTRACT

$LaNiO_3$ perovskites have been recently studied for H_2 production from NH_3 decomposition / cracking. So far, this material has had its catalytic performance boosted along the addition of basic doping agents. Nevertheless, little attention has been paid to the potential benefit to gain from its textural properties. In this work, high specific surface area $LaNiO_3$ were prepared through the yet never explored combination of citric acid as complexing agent, SBA-15 as sacrificial hard template (to create mesopores), and exsolution (to expose and activate Ni). After removal of the template, the resulting mesoporous $LaNiO_3$ reached a specific surface area as high as 200 m^2/g. In a second step, Ni nanoparticles were exsolved to reach the final catalyst, yielding 89 % NH_3 conversion at 550 °C and a GHSV of 30 000 $mL/g_{cata}.h$, with a stability of at least 72 h. Due to the extended specific surface area of $LaNiO_3$, exsolved Ni nanoparticles were highly dispersed which greatly enhanced the catalytic performance. This catalyst achieved a H_2 formation rate of 29 $mmol/g_{cata}.min$ which is higher than any previously reported doped $LaNiO_3$. This work demonstrates the feasibility to produce both noble metal and promoter-free $LaNiO_3$ being particularly active and stable in efficient H_2 production from NH_3 decomposition.

1. Introduction

For more than a century, worldwide societies have grown and developed using a carbon-based energy industry [1]. Although fossil fuels have brought welfare and progress to our economies, it has not been the same for the environment [1,2]. Global warming, depletion of fossil fuels sources and air pollution are among the most important current issues. To mitigate these environmental problems, it is necessary to find new, eco-friendly energy sources [2,3]. In this regard, H_2 with an energy density three times higher than diesel or gasoline (120 MJ/kg vs 46 MJ/kg), appears as a green energy source which can replace traditional carbon fuels in the upcoming decades [3]. Despite its superior energy density, drawbacks associated with hydrogen handling, storage (i.e. liquefaction at −253 °C or at 500 bars) and safe distribution, have prevented the development of an efficient hydrogen based economy [2–4]. In this context, several hydrogen carriers such as metal hydrides, H_2O and NH_3 have been proposed as alternatives for H_2 storage and *in situ* production [5–7]. Among them, NH_3 arises as one of the most promising [7].

NH_3 possesses a high hydrogen content (17.7 %wt) which provides several solutions to the above-mentioned inconvenients [4,7]. NH_3 can be stored easier than pure H_2 as a liquid (with its liquefaction at only –33.4 °C or 8.5 bars), indeed [7,8]. In addition, NH_3 is a stable molecule with a low explosibility which makes it safer for transportation [7–9]. Apart from H_2 and N_2 formation, NH_3 decomposition does not emit any greenhouse gas which is beneficial for our polluted environment [8,9]. NH_3 cracking into H_2 and N_2 is an endothermic and reversible reaction that, without the presence of an appropriate catalyst, the reaction requires high temperatures beyond 800 °C to achieve a complete conversion [10]. Thereby, active heterogeneous catalysts are required to decrease the reaction temperature without sacrificing conversion and diminishing the energy input [10,11].

The catalytic decomposition of NH_3 involves its adsorption on the catalyst surface (Eq. (1)) followed by the breaking of N-H bonds (Eqs.

* Corresponding author at: Institute of Condensed Matter and Nanosciences (IMCN), Université catholique de Louvain, Place Louis Pasteur 1. L04.01.09, 1348 Louvain-la-Neuve, Belgium.
E-mail address: sebastian.gamez@uclouvain.be (S. Gamez).

https://doi.org/10.1016/j.cej.2025.160377
Received 12 November 2024; Received in revised form 19 January 2025; Accepted 5 February 2025
Available online 8 February 2025

(2)–(4)). Then, the associative recombination of $N_{(ads)}$ (Eq. (5)) and $H_{(ads)}$ (Eq. (6)) atoms occurs to form diatomic H_2 and N_2, respectively. As regards Eq. (5), which is the rate limiting step of the reaction, a transition metal-nitrogen bond (M−N) is formed on the catalyst surface [12,13]. This bond should be weakened to form the triple N≡N bond during the associative recombination of $N_{(ads)}$ atoms. The latter can be accomplished by increasing the electron donation from the transition metal to the M−N antibonding orbital using either a basic support or a dopant that boosts catalysts basicity. This electron-donation can activate the N≡N triple bond formation at lower temperatures which leads to an energy-saving process to produce H_2 from NH_3 [13].

$$NH_{3(g)} \rightarrow NH_{3(ads)} \quad (1)$$

$$NH_{3(ads)} \rightarrow NH_{2(ads)} + H_{(ads)} \quad (2)$$

$$NH_{2(ads)} \rightarrow NH_{(ads)} + H_{(ads)} \quad (3)$$

$$NH_{(ads)} \rightarrow N_{(ads)} + H_{(ads)} \quad (4)$$

$$N_{(ads)} + N_{(ads)} \rightarrow N_{2(ads)} \quad (5)$$

$$H_{(ads)} + H_{(ads)} \rightarrow H_{2(ads)} \quad (6)$$

In the literature, most of the catalysts employed for NH_3 decomposition are Ru based ones that reach complete conversions at 550 °C [14,15]. For instance, Zhang *et al.* deposited Ru on La_2O_3 to achieve 90 % conversion at 525 °C under a gas hourly space velocity (GHSV) of 18 000 mL_{NH3}/g_{cata}.h [14]. Similarly, Zhiqiang *et al.* used Ru nanoparticles supported on $KSiO_3$ and accomplished complete conversion at 550 °C at 30 000 mL_{NH3}/g_{cata}.h keeping the same catalytic activity for 70 h [15]. However, the high cost of Ru and its scarcity have prompted researchers to look for non-noble metal catalysts that are as active as Ru ones. Among the different transition metals available, several exploratory investigations have identified Ni as a potential candidate to substitute Ru [16]. Nevertheless, most of Ni catalysts reported in the literature require high temperatures to completely decompose NH_3 (T > 550 °C) and most of them are not stable after a few hours of reaction due to Ni sintering [17,18].

To better exploit Ni, several authors have included this non-noble metal in an ABO_3 type perovskite structure. The latter is known to possess high electron conductivity and high chemical stability over a wide range of temperature which is essential to prevent Ni sintering under catalytic reaction conditions [19,20]. Within ABO_3, the "A" trivalent cation is a rare earth metal while the "B" divalent cation is a non-noble transition metal. The salt precursors of these cations are dissolved together followed by a precipitation to obtain a mixture of oxides. Then, a calcination step at high temperatures (T > 750 °C) is applied leading to low specific surface area perovskites (~ 4 m^2/g) [21–23]. Among all ABO_3 solids, $LaNiO_3$ has proven to be quite active in NH_3 decomposition [21,22]. For instance, Podila *et al.* managed to reach 90 % conversion at 550 °C and under 6 000 mL_{NH3}/g_{cata}.h. To improve the catalytic performance of $LaNiO_3$, authors have added dopants in the perovskite structure to increase its basicity. For instance, Li *et al.* have prepared $La_{0.5}Sr_{0.5}NiO_3$ that achieved 88 % conversion at 550 °C and under 30 000 mL_{NH3}/g_{cata}.h, keeping the same conversion for 50 h [23]. Although the catalytic activity is comparable to that of Ru catalysts, the latter perovskite presents a low specific surface area (~12 m^2/g) just like many other perovskites reported in the literature. Therefore, such perovskite catalysts need to be further improved.

To the best of our knowledge, boosting the efficiency of $LaNiO_3$ in NH_3 decomposition by specifically fostering its specific surface area has never been reported. Conventional techniques such as the self-combustion method, precipitation or the citric acid complexing method yield $LaNiO_3$ with low specific surface areas due to sintering during the calcination step, indeed. Hence, in this work, we propose to prepare the catalyst along the yet never explored combination of the citric acid complexation method, sacrificial hard templating with SBA-15, and subsequent Ni exsolution to yield highly dispersed Ni nanoparticles on a high specific surface area Ni and La based perovskite catalyst. The combined excellent textural properties and high Ni dispersion of our materials lead to an efficiency and a stability in the catalytic NH_3 decomposition never reached before for clean H_2 production from ammonia on both noble metal-free and promotor-free catalysts.

2. Experimental section

Bulk $LaNiO_3$ was synthesized as a reference material, while mesoporous SBA-15 was used as sacrificial hard template to deposit $LaNiO_3$ precursors. SBA-15 bears higher thermal and hydrothermal stability than other silicate materials with large unit cell size to yield wide pores [24,25]. After SBA-15 was eliminated from $LaNiO_3$ structure, high specific surface area perovskites were produced. In a final step, an exsolution under reducing conditions was applied to expose and activate Ni nanoparticles at the surface of the catalysts.

2.1. Synthesis of bulk $LaNiO_3$

Bulk $LaNiO_3$ perovskite was synthesized through the citric acid complexing method.[23-25] First, 8 mmol of nickel nitrate hexahydrate (2.37 g $Ni(NO_3)_2{\cdot}6H_2O$, 98 %, Alfa Aesar) and 8 mmol of lanthanum nitrate hexahydrate (3.46 g of $La(NO_3)_3{\cdot}6H_2O$, 99.99 %, Sigma-Aldrich) were dissolved in 30 mL of ethanol (CH_3OH, 96 %, Carl Roth) and 10 mL of distilled H_2O. Next, 3.07 g of citric acid ($C_6H_8O_7$, 98 %, TCI Chemicals) was added to the previous solution to keep a Ni:La:citric acid ratio of 1:1:2. The solution was magnetically stirred at room temperature for 30 min followed by another 12 h of agitation at 60 °C. The green spongy solid obtained was then dried at 110 °C for another 12 h and then calcined in air at 750 °C for 4 h with a heating ramp of 2 °C/min to obtain the $LaNiO_3$ perovskite structure.

2.2. Synthesis of SBA-15

Mesoporous SBA-15 was synthesized by a hydrothermal method using poly(ethylene glycol)-block-poly(propylene glycol)-block-poly (ethylene glycol) (Pluronic P123, Sigma-Aldrich) as a soft template. Briefly, 2.82 g of P123 was dissolved in 75 mL of distilled H_2O along with 14 mL of HCl (37 %, Sigma-Aldrich). The mixture was magnetically stirred for 2 h at 35 °C until all P123 was well dissolved. Next, 6.6 mL of tetraethyl orthosilicate (TEOS, $C_8H_{20}O_4Si$, >98 %, TCI Chemicals) was added to the previous mixture and the agitation continued at 35 °C for 12 h. The solution was then transferred into a Teflon-lined stainless-steel autoclave and heated under autogenous pressure at 90 °C for 48 h. The precipitate obtained was vacuum-filtered and washed 3 times with 25 mL of hot (~85 °C) distilled water. Finally, the solid was calcined at 550 °C for 4 h under air.

2.3. Synthesis of high specific surface area $LaNiO_3$

SBA-15 was employed as a sacrificial hard templating agent to distribute the La and Ni precursors over its structure. Precisely, 4 mmol of $Ni(NO_3)_2{\cdot}6H_2O$ and 4 mmol of $La(NO_3)_3{\cdot}6H_2O$ were dissolved together in 30 mL of ethanol and 10 mL of distilled H_2O. Afterwards, 8 mmol of citric acid was added to the previous solution and magnetically stirred for 30 min at room temperature. Next, different amounts of SBA-15 (i.e. 0.25, 0.50 and 1.00 g) were added to the mixture and the resulting suspension was agitated for 4 h at 60 °C. The solvent was then removed through rotary evaporation at 70 °C. The green solid obtained was dried overnight at 110 °C followed by calcination at 750 °C under air for 4 h with a heating ramp of 2 °C/min. To remove SBA-15 and just leave the $LaNiO_3$ phase, the calcined solid was suspended into 80 mL of a 5 mol/L NaOH solution. The suspension was magnetically stirred for 12

h at 90 °C to dissolve SBA-15. Finally, the lanthanum nickelate oxide without SBA-15 was vacuum-filtered and washed three times with 25 mL of distilled H_2O at 85 °C, followed by drying in the hood overnight at room temperature. Prior to catalytic tests, all samples were submitted to a reducing exsolution protocol flowing them with 100 mL/min of H_2/Ar (5 v/v%) at 550 °C (according to H_2-TPR analysis Fig. S1) for 1 h using a heating ramp of 5 °C/min (Scheme 1).

For sake of clarity Ni-La_2O_3 is written in the scheme, but actually it should be written Ni_x-$LaNi_{1-x}O_y$ as likely not all the Ni is exsolved (some of it likely remaining in the perovskite). Moreover, the symbol – is purposedly used instead of / to suggest the fact Ni particles are somehow embedded in the perovskite and therefore resistant to sintering, whereas / is conventionally used to represent particles just deposited at the surface of a support.

Hereafter bulk perovskite is named as $LaNiO_3$-B, while after reduction treatment it is denoted as R-$LaNiO_3$-B. The samples synthesized with 1.00, 0.50 and 0.25 g of SBA-15 are denoted $LaNiO_3$-SBA15(1.00 g), $LaNiO_3$-SBA15(0.50 g) and $LaNiO_3$-SBA15(0.25 g). After the hard template removal, samples are named $LaNiO_3$-S(X) with X being the mass of SBA-15 previously used for their synthesis. Finally, the prefix "R" refers to the samples treated under H_2, for instance R-$LaNiO_3$-S(X) with X being the mass of SBA-15 that was initially introduced.

2.4. Characterization techniques

Textural properties of $LaNiO_3$ samples were studied by N_2 physisorption at −196 °C using a Micromeritics Tristar 3000 machine. Prior to analyses, about 100 mg of samples was degassed under vacuum (~0.1 mbar) at 200 °C for 12 h. The specific surface area was calculated by means of the Brunauer-Emmet-Teller (BET) method exploiting the data collected in the $0.05 < P/Po < 0.30$ range of the adsorption branch isotherm. Pore volume and pore size distributions were estimated along the Barrett, Joyner and Halenda method (BJH) using the data of the desorption branch [26–28]. The morphology of perovskites after SBA-15 removal was analyzed through scanning electron microscope (SEM) in a JEOL JSM-7600F equipment with an accelerating voltage of 0.1 kV to 30 kV.

To confirm the formation of the lanthanum nickelate oxide phase and exsolved Ni nanoparticles, X-ray diffraction (XRD) was performed in a Bruker-D8 Advance diffractometer with a Bragg-Brentano geometry and a copper anode Kα = 0.15418 nm operated at 20 kV and 5 mA. Grinded $LaNiO_3$ samples before and after reduction in H_2 were placed on polished silicon sample holders previously coated with a thin layer of Nivea cream. Diffractograms were recorded from $5° < 2\theta < 80°$ with 0.015° increments in 26 min. Phase identification was performed with the ICDD-PDF2–2004 database. Metallic Ni crystallite size was determined through Sherrer. The reflection from the (111) plane, occurring at $2\theta = 44.5°$ (the most intense peak from Ni pattern) was used for the crystallite size measurement. Pure Ni powder with a crystallite size of 100 nm was employed as reference for all calculations.

$$d = \frac{K\lambda}{\beta Cos\theta} \tag{7}$$

Where d corresponds to crystalline size, K represents the Scherrer constant (0.98), λ is the wavelength (1.54) while β denotes the full width at half maximum of the selected peak.

Ni nanoparticles size distribution after exsolution was assessed through High resolution transmission electron microscopy (HRTEM) using a JEOL 2100 Plus UHR microscope operating at 200 kV. Scanning transmission electron microscopy (STEM) images using a high-angle annular dark-field (HAADF) detector were also acquired. Chemical mapping was performed with an energy dispersive X-ray (EDX, Oxford Instruments X-Max 80 SDD) spectrometer attached to the microscope column.

Elemental composition and Ni oxidation state on the surface of the samples were assessed by X-ray photoelectron spectroscopy (XPS) in a SSX 100/206 photoelectron spectrometer (Surface Science Instruments USA). The machine is equipped with a monochromatized micro focused Al X-ray source powered at 20 mA and 10 kV. Grinded samples of $LaNiO_3$ before and after reduction treatment under H_2 were placed in 4 mm stainless steel troughs. Afterwards, the troughs were collocated on a ceramic carousel covered by a Ni grid. After a degassing step under 10^{-7} Pa for 12 h, all samples were transferred to the analysis chamber under 10^{-9} Pa with the flood gun set at 8 eV and an analysis angle of 55°. Elemental composition was acquired after a survey scan. The following sequence of spectra was recorded: survey spectrum, C 1 s, O 1 s, La 4d

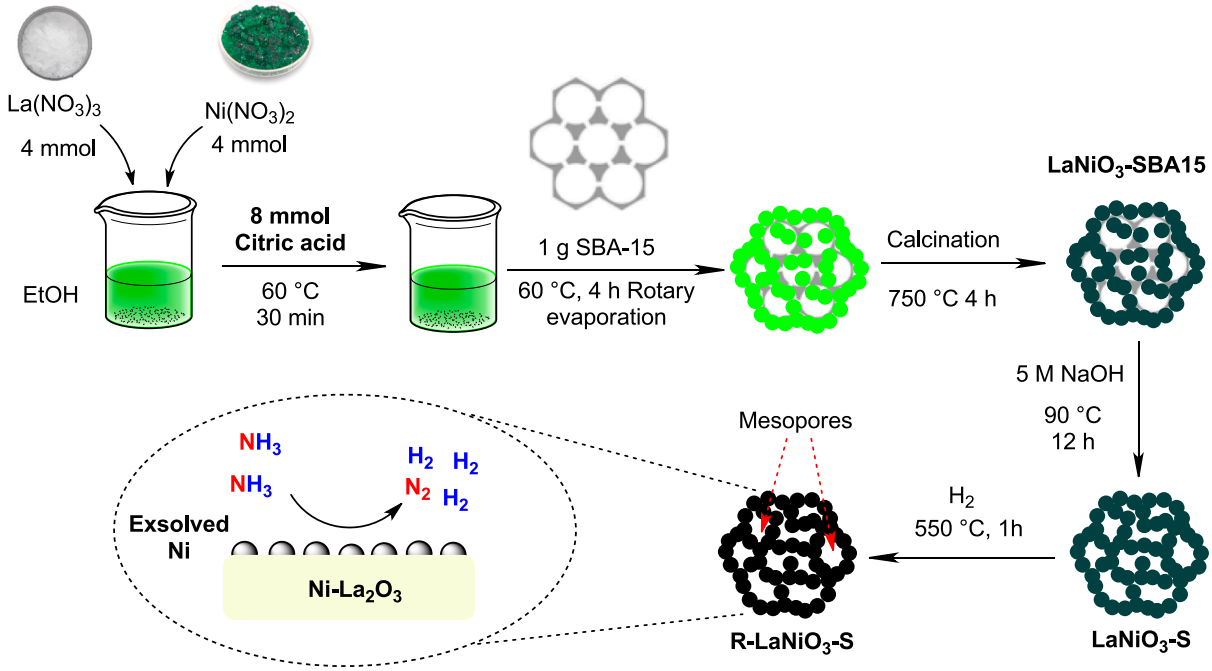

Scheme 1. Synthesis of high specific surface area Ni-exsolved $LaNiO_3$ perovskites for NH_3 decomposition.

and Ni 3p. Ni 3p core level was chosen for Ni oxidation state estimation since La $3d_{3/2}$ and Ni $2p_{3/2}$ peaks overlap, making difficult to disentangle the different La and Ni contributions. Data processing was carried out by means of the CasaXPS program (Casa Software Ltd, UK). The C-(C,H) contribution of the C 1 s peak was set at 284.8 eV as a reference to calibrate all recorded spectra. For the peaks fitting a Shirley background was employed with a Gaussian/Lorentzian (30/70) product function and after subtraction of a non-linear baseline.

Ni metallic surface area and dispersion on reduced perovskites was estimated by H_2 chemisorption in a Microtrac Belcat II analyzer. For this purpose, around 100 mg of Ni-exsolved $LaNiO_3$ samples was first degassed at 150 °C for 3 h in a He constant flow of 50 mL/min. Next, samples were heated up to 600 °C under a mixture of 20 mL/min of H_2 and 30 mL/min of He. The temperature was kept for 1 h and then samples were cooled down to 50 °C under a 50 mL/min flow of Ar. Afterwards, pulses of 0.5 mL of a 0.5 v/v% H_2 dissolved in Ar were injected to the reduced samples. The H_2 volume consumed was measured with a thermal conductivity detector (TCD) while a Ni:H ratio of 1 was assumed to calculate the metallic surface area [30,31].

2.5. Catalytic tests

Catalytic tests were performed in a fixed bed reactor (Volume = 0.12 cm^3, ID = 7 mm) at atmospheric pressure. First, $LaNiO_3$ perovskites were reduced under 100 mL/min of H_2/Ar (5 v/v%) at 550 °C for 1 h to exsolve Ni. Then, the reduced $LaNiO_3$ was cooled down to 300 °C under N_2 atmosphere. At that point, 100 vol% NH_3 as fed inside the reactor to reach a GHSV = 30 000 mL/g_{cata}.h. The reactor temperature was raised by intervals of 50 °C up to 650 °C keeping the same temperature for at least 2 h·NH_3 conversion and H_2 formation rate was estimated with an online gas chromatograph (Global Analyser Solutions CompactGC 4.0) equipped with a Rt-Q-BOND 15 m x 0.32 mm column and two TCD detectors (one focused for H_2 and N_2 detection and the other for NH_3). The activation energy was estimated by keeping NH_3 conversion below 20 % at different temperatures. Finally, a stability test was performed at 550 °C for 72 h under a GHSV of 30 000 mL/g_{cata}.h.

3. Results and discussion

Fig. 1a shows the X-Ray diffractograms of $LaNiO_3$-B and $LaNiO_3$-S samples before the reducing treatment. All samples display peaks at 23.3° (101), 32.9° (110), 40.6° (021), 41.2° (003), 47.4° (202), 53.7° (211), 58.8° (122), 69.7° (220) and 78.9° (312), a pattern which corresponds to rhombohedral $LaNiO_3$ perovskite (PDF 79–2451) [22,23]. On the other hand, the diffractogram of SBA-15 (Fig. S2a) displays broad peaks at 23° and 63° characteristic of the SBA-15 structure [32,33]. The former large peak is still a bit visible on $LaNiO_3$-SBA15 diffractograms (i.e. before removal of the SBA, Fig. S1b) which also presents the characteristic peaks of $LaNiO_3$. All of this evidences that i) the $LaNiO_3$ phase was successfully formed during the calcination stage without interference of the silicon oxide material, and 2) SBA-15 removal by NaOH washing does not alter $LaNiO_3$, that remained the only phase detected.

Table S1 compiles the crystallite sizes of synthesized $LaNiO_3$-S perovskites. The sample prepared with 1.00 g of SBA-15 presented the smallest crystallite size. The connection between the decrease in $LaNiO_3$ crystallite size and the increase in SBA-15 amount can be explained by the fact that greater amounts of the hard template provided more space for a better distribution of La and Ni ions. Then, during the calcination stage, less agglomeration occurred which resulted in $LaNiO_3$ with smaller crystallite sizes.

After the reducing treatment under H_2/Ar (5 v/v%), $LaNiO_3$ peaks vanished (Fig. 1b). As a counterpart, new peaks appeared, belonging to La_2O_3 (PDF 74–2430) and metallic Ni (PDF 65–2865) phases, confirming the exsolution of the latter. This transformation is the consequence of $LaNiO_3$ decomposition into oxygen deficient phases such as $LaNiO_{2.7}$, $LaNiO_{2.5}$ and finally La_2NiO_4 in a reducing atmosphere [34,35]. Through oxygen vacancies of such phases, Ni atoms start to diffuse towards the surface of the solid. As more Ni atoms migrate to the surface, they agglomerate, forming nanoparticles [34,35]. Note that the presence of residual Ni remaining within the La_2O_3 matrix is not excluded. The higher the temperature is, the bigger the obtained Ni nanoparticles are, as a result of a bigger accumulation of exsolved Ni and the subsequent growth of the nanoparticles [34,35]. As regards La_2NiO_4, it is finally decomposed by H_2 yielding La_2O_3 and Ni as follows [36]:

$$LaNiO_{3(s)} + H_{2(g)} \xrightarrow{400-500^\circ C} La_2NiO_{4(s)} + Ni_{(s)} + H_2O_{(g)} \quad (8)$$

$$La_2NiO_{4(s)} + H_{2(g)} \xrightarrow{500-600^\circ C} La_2O_{3(s)} + Ni_{(s)} + H_2O_{(g)} \quad (9)$$

Among the reduced samples, R-$LaNiO_3$-B displays peaks at 36.8° (111) and 43.4° (200) that correspond to NiO (PDF 89–3080). This suggests that not all Ni was reduced by H_2 during the reduction process. Conversely, R-LaNiO-S samples only display a broad peak at 44.6°, attributed to metallic Ni nanoparticles over the newly formed La_2O_3 phase. As regards metallic Ni crystallite sizes, R-$LaNiO_3$-B presents Ni crystals around 13 nm, whereas the smallest crystallite size is shown by R-$LaNiO_3$-(1.00 g) around 8 nm (Table S1). The integration of SBA-15 in the synthesis (and then its removal) thus allowed to reach metallic Ni nanoparticles with small sizes.

The presence of NiO on R-$LaNiO_3$-B and not in R-$LaNiO_3$-S samples can be explained by the fact that SBA-15 allowed a better dispersion of $LaNiO_3$. This in turn facilitated Ni diffusion through the La-containing phases and its reduction by H_2. In the case of R-$LaNiO_3$-B, not all Ni was exposed to H_2 and some atoms could combine with lattice oxygen of the pristine perovskite yielding NiO. The latter can easily be reduced by

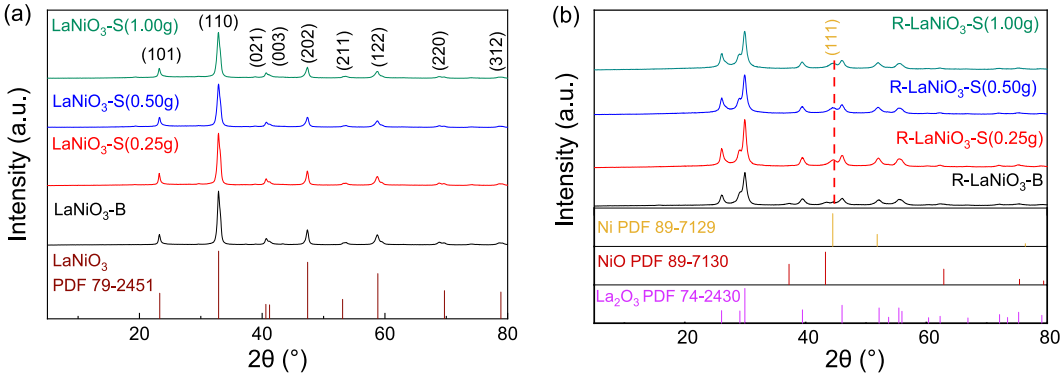

Fig. 1. X-Ray diffractograms of $LaNiO_3$ samples (bulk and after removal of SBA template) a) before reduction and b) after reduction under H_2/Ar (5 v/v%) at 550 °C for 1 h.

H_2 but in the case of R-$LaNiO_3$-B, some NiO nanoparticles still remained on La_2O_3 surface, likely because being too big.

N_2 physisorption isotherms of synthesized $LaNiO_3$ perovskites are shown in Fig. 2 and S2. $LaNiO_3$-B displays a type 2 isotherm with a narrow hysteresis loop at $P/P^\circ = 0.9$ (Fig. 2a). This isotherm shape is characteristic of macroporous/non-porous materials with a low specific surface area which in the case of $LaNiO_3$-B is around 4 m^2/g (Table 1). This value lies within the normal range of bulk $LaNiO_3$ (1–20 m^2/g) reported in the literature [21,22].

Pure SBA-15 displays a type IV isotherm with a H1 hysteresis loop (which is characteristic of mesoporous materials) at $P/P^\circ = 0.60$. Its pore size distribution is centered at 5.4 nm (Figs. S3a and b). $LaNiO_3$-SBA15 samples also show type IV isotherms but with hysteresis loops located at lower P/P° and extending from 0.40 to 0.60, which can be interpreted as due to the coating of perovskites inside SBA-15 mesopores, inducing a decrease of SBA pore sizes (Figs. S3c and d). This is precisely observed in the pore size distribution graphics (Fig. S3d) where the mean pore diameter diminished from 5.4 nm for the pristine SBA-15 down to 4.0 nm in the case of $LaNiO_3$-SBA15(0.25 g). In the latter, a greater number of pores are filled by La and Ni precursors decreasing pore sizes of SBA-15. On the other hand, in $LaNiO_3$-SBA15(1.00 g) less pores are filled by the same precursors and therefore the pore size distribution does not diminish so markedly in comparison to pure SBA-15. In addition, TEM analysis confirmed the deposition of $LaNiO_3$ inside SBA-15 matrix. Fig. S4a and b show aggregated particles of $LaNiO_3$ with uneven spherical shape around SBA-15 surface. This asseveration was confirmed through EDS chemical mapping (Fig. S4c) where Si enriched zones remain surrounded by an La and Ni atoms belonging to $LaNiO_3$. When SBA-15 is removed through NaOH washing, the texture of $LaNiO_3$-S changed compared to $LaNiO_3$-SBA-15 samples. Lower specific surface areas are obtained with broader pore size distributions. The broad pore size distribution reflects that likely the perovskite had initially formed inside both the meso- and macroporosity of the SBA-15. $LaNiO_3$-S(1.00 g) displays the largest specific surface area (i.e. 201 m^2/g) achieved by any perovskite reported in this work or in the literature. Most of $LaNiO_3$ synthesized through other methodologies such as sol–gel or self-combustion method reach specific surface areas of about 20 m^2/g to the best [21,37].

Even other strategies based on the addition of basic promoters like alkaline earth cations (i.e. Ca or Sr) to simultaneously increase

Table 1
Textural properties of synthesized perovskites.

Sample	Specific surface area (m^2/g)[a]	External surface area (m^2/g)[b]	Pore volume (cm^3/g)[c]	Mean Pore diameter (nm)[c]
$LaNiO_3$-B	4	4	0.01	42.6
R-$LaNiO_3$-B	4	4	0.01	43.7
SBA-15	926	8	0.99	5.4
$LaNiO_3$-SBA15 (0.25 g)	80	5	0.08	4.0
$LaNiO_3$-SBA15 (0.50 g)	144	7	0.14	4.5
$LaNiO_3$-SBA15 (1.00 g)	222	6	0.21	5.2
$LaNiO_3$-S (0.25 g)	50	36.5	0.08	8.4
$LaNiO_3$-S (0.50 g)	97	35	0.12	5.6
$LaNiO_3$-S (1.00 g)	201	37	0.20	4.6
R-$LaNiO_3$-S (0.25 g)	34	34	0.07	11.6
R-$LaNiO_3$-S (0.50 g)	60	40	0.09	6.7
R-$LaNiO_3$-S (1.00 g)	138	44	0.18	4.9

[a] BET equation; [b]t-plot method; [c]BJH method.

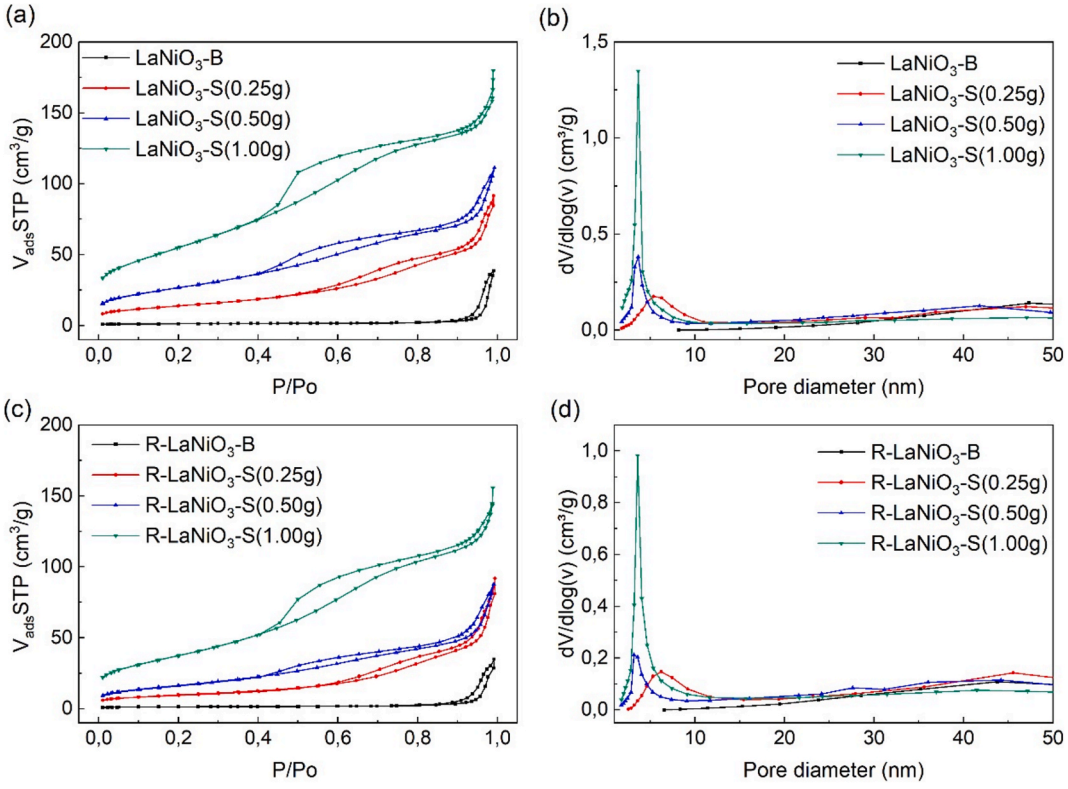

Fig. 2. N_2 adsorption–desorption isotherms of $LaNiO_3$ samples a) before reduction and c) after reduction in H_2/Ar (5 v/v%) at 550 °C for 1 h; Pore size distribution curves of $LaNiO_3$ b) before reduction and d) after reduction in H_2/Ar (5 v/v%) at 550 °C for 1 h.

perovskites basicity and induce deficiencies in the $LaNiO_3$ lattice never led to specific surface areas higher than 40 m^2/g [22,23]. In contrast, our $LaNiO_3$-S can easily overtake those low specific surface areas without modifying the structure of the lanthanum nickelate oxide phase.

As regards the morphology of synthesized perovskites, Fig. 3 show SEM images of samples after SBA-15 removal and bulk $LaNiO_3$ as reference. The latter presents a smooth surface compared to modified perovskites. Conversely, $LaNiO_3$-S(X) shows surfaces with more defects which increases the surface area available for the catalytic reaction. These images show evidence of SBA-15 influence during the synthesis steps. The hard template not only permitted an increase in surface area but also contributed to produce catalysts with rough surface. Thereby, a surface with more defects can impact positively the catalytic performances in NH_3 decomposition due to more area available for the reaction.

Since $LaNiO_3$ is not the active phase in NH_3 decomposition, the textural properties of our synthesized samples were investigated after the reducing exsolution treatment in H_2-containing atmosphere. In all cases the same shape of the N_2 physisorption isotherms were obtained (Fig. 2) but with moderately lower specific surface areas (Table 1).

As suggested by the reduction of pore volume of the exsolved samples and the increase of the mean pore diameter (more significantly observed when less SBA-15 was used), this decrease of specific surface area can be explained by the blocking of the smallest pores during the exsolution of Ni atoms outward the lanthanum oxide phase. Despite the loss of specific surface area by plugging the smallest pores, in the case of $LaNiO_3$-S(1.00 g) samples this phenomenon is not too pronounced (because presenting before exsolution a higher proportion of big pores than the two samples made from smaller SBA-15 amounts) and the average pore size is kept around 4.9 nm with a final unprecedented specific surface area of 138 m^2/g.

XPS analyses were performed to estimate Ni oxidation state through the assessment of Ni 3p high resolution spectra (Fig. 4). Ni^0, Ni^{2+} and Ni^{3+} species can be distinguished indeed as giving different 3p contributions at 65.5, 66.7 and 68 eV, respectively [29,38]. Before reduction in H_2/Ar (5 v/v%), the synthesized $LaNiO_3$ samples display only Ni^{2+} and Ni^{3+} ions. Since only $LaNiO_3$ phase was detected through XRD, the presence of Ni^{2+} ions can be attributed to small amounts of NiO that do not belong to the perovskite structure. After H_2 treatment, Ni^{3+} content diminished greatly in favor of Ni^0 because of $LaNiO_3$ transformation into La_2O_3 and exsolved Ni nanoparticles.

XPS spectra also demonstrate that not all Ni is reduced and therefore higher reduction temperatures could be applied to completely reduce Ni^{3+} into Ni^0. However, an increase in temperature can also lead the exsolved Ni nanoparticles to further grow causing an undesired decrease in Ni dispersion as compared to what can be obtained for the same extent of exsolution at lower temperature.

Table 2 recaps the surface elemental composition of the four perovskites assessed in this work before and after exsolution. In all cases the total amount of Ni increased as a consequence of Ni species migration from inside the perovskite matrix towards the outer surface.

This increase in Ni content confirms that exsolution took place during the reducing treatment in H_2/Ar (5 v/v%) and is consistent with XRD data. In addition, in $LaNiO_3$-S samples there is still the presence of silicon in spite of the fact that all perovskites were thoroughly washed with NaOH solutions. In this regard, Table S2 that shows the elemental

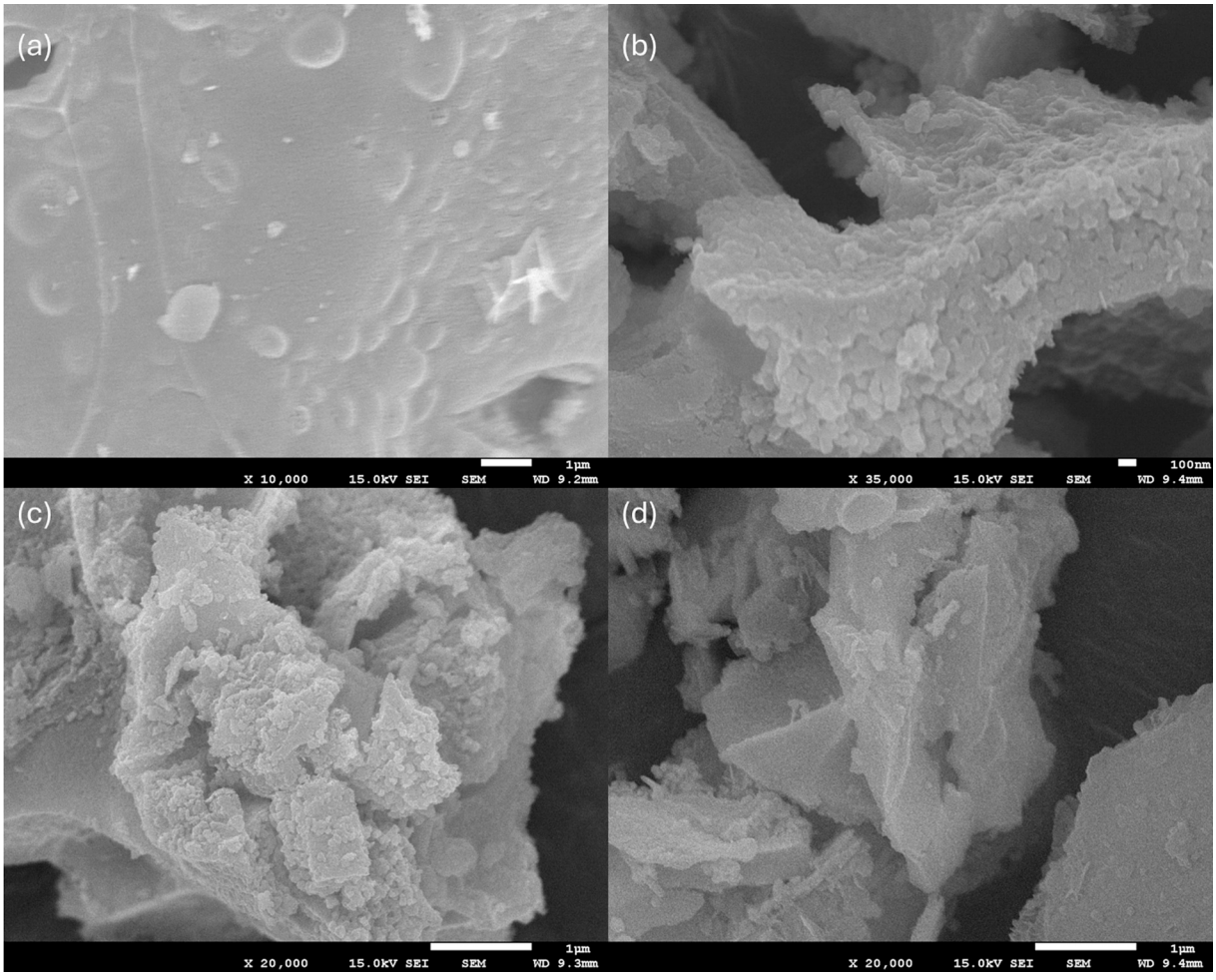

Fig. 3. SEM images from: a) $LaNiO_3$-B; b) $LaNiO_3$-S(0.25 g); c) $LaNiO_3$-S(0.50 g); $LaNiO_3$-S(1.00 g).

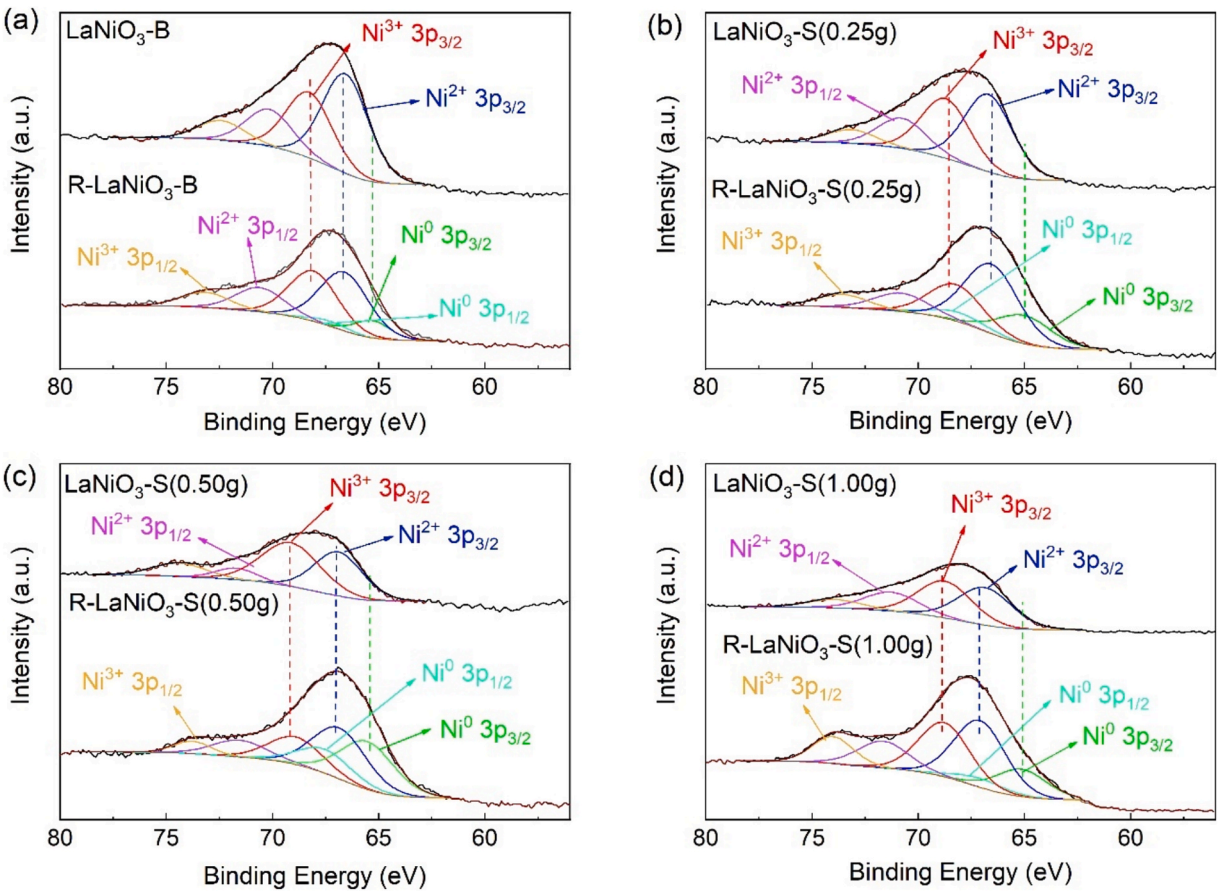

Fig. 4. High resolution spectra of Ni 3p from a) $LaNiO_3$-B before and after exsolution; b) $LaNiO_3$-S(0.25 g) before and after reduction; c) $LaNiO_3$-S(0.50 g) before and after exsolution; d) $LaNiO_3$-S(1.00 g) before and after exsolution.

Table 2
Elemental composition by XPS (in wt%) of perovskites before and after exsolution.

Sample	C (%)	O (%)	Si (%)	La (%)	Ni (%) Ni^{2+}	Ni^{3+}	Ni^0	Ni	Ni/La
$LaNiO_3$-B	7.8	32.0	––	47.5	7.7	5.1	––	**12.7**	**0.27**
$LaNiO_3$-S(0.25 g)	13.6	37.8	3.3	33.5	6.7	5.1	––	**11.8**	**0.35**
$LaNiO_3$-S(0.50 g)	7.7	35.2	3.7	36.5	7.7	9.2	––	**16.9**	**0.46**
$LaNiO_3$-S(1.00 g)	9.9	42.5	3.0	28	8.4	8.2	––	**16.6**	**0.59**
R-$LaNiO_3$-B	9.5	34.2	––	45.8	5.1	4.3	1.1	**10.5**	**0.23**
R-$LaNiO_3$-S(0.25 g)	12.9	33.2	3.2	32.0	9.7	5.1	4.0	**18.8**	**0.59**
R-$LaNiO_3$-S(0.50 g)	8.3	34.4	3.9	33.1	10.4	4.6	5.3	**20.3**	**0.61**
R-$LaNiO_3$-S(1.00 g)	8.6	37.2	3.1	30.2	5.6	7.4	7.9	**20.9**	**0.69**

composition of samples before and after SBA-15 removal, confirms that the Si content was reduced greatly after the washings with NaOH. Therefore, the amount of Si that remains on $LaNiO_3$-S samples are just traces of the hard template that was not removed.

From XPS analysis it is clear that all R-$LaNiO_3$-S samples showed a greater amount of Ni^0 than R-$LaNiO_3$-B. Hence, a greater number of active sites are present on R-$LaNiO_3$-S surface and available for NH_3 decomposition. These results also confirm what was observed by XRD and N_2 physisorption. The small crystallites of $LaNiO_3$ formed thanks to the integration of SBA-15 in the synthesis were better exposed to reduction under H_2 which in turn transformed more Ni ions into metallic Ni than in the other samples, especially in the reference perovskite (i.e. $LaNiO_3$-B).

Ni specific surface area and Ni dispersion from all samples were assessed by means of H_2 chemisorption (Table 3). R-$LaNiO_3$-B shows a Ni specific surface area = 4.5 m^2/g which agrees to other Ni-exsolved bulk $LaNiO_3$ reported in the literature [31]. On the other hand, R-$LaNiO_3$-S samples displayed greater Ni specific surface areas which can be explained due to the large specific surface areas of the synthesized materials provided by SBA-15. Thanks to the created mesopores, a high

Table 3
Ni particle size and dispersion over reduced perovskites.

Catalyst	Ni particle size (nm)[a]	Ni surface area (m^2/g)[b]	Ni dispersion (%)[b]
R-$LaNiO_3$-B	12.0 ± 1.9	4.5	0.67
R-$LaNiO_3$-S (0.25 g)	11.6 ± 2.0	5.9	0.88
R-$LaNiO_3$-S (0.50 g)	7.5 ± 1.5	11.7	1.75
R-$LaNiO_3$-S (1.00 g)	7.0 ± 2.5	19.5	2.92

[a] TEM analysis; [b]H_2 chemisorption

specific surface area was developed after the calcination stage. Then, Ni nanoparticles had more space to well distribute throughout the La_2O_3 interface which led to smaller Ni nanoparticles. Thus, the higher the amount of SBA-15, the higher the surface area and then the greater the Ni dispersion achieved. This was correlated to Ni dispersion where samples with larger specific surface areas displayed higher Ni dispersions. For instance, R-$LaNiO_3$-S(1.00 g), presented a Ni dispersion 4 times higher than in the case of R-$LaNiO_3$-B.

Dispersion results were also consistent with Ni nanoparticle sizes assessed through TEM. The TEM image in Fig. 5a displays Ni nanoparticles distributed on bulk R-$LaNiO_3$-B surface with a mean diameter around 12 nm. This value agrees with other results reported for Ni-exsolved bulk $LaNiO_3$ in the literature [22,23]. As regards the samples synthesized with SBA-15, Ni nanoparticle sizes decreased as the content of SBA-15 increased (Fig. 6a, Fig. S5a and Fig. S6a). Hence a greater amount of the hard template facilitated a better distribution of $LaNiO_3$ which in turn yielded small Ni nanoparticles after exsolution.

HRTEM images from R-$LaNiO_3$-B and R-$LaNiO_3$-S(1.00 g) catalysts (Fig. 5b and Fig. 6b) show two types of lattice fringes: 0.20 nm that corresponds to metallic Ni (1 1 1) and 0.30 nm ascribed to La_2O_3 (002). The same lattice fringes were also found on HRTEM images from R-$LaNiO_3$-S(0.25 g) and R-$LaNiO_3$-S(0.50 g) samples (Fig. S3b and Fig. S4b), which is consistent with XRD results. In addition, Fig. 6b shows the presence of mesopores which is the evidence that SBA-15 removal created mesoporosity in $LaNiO_3$ structure. Thus, Ni nanoparticles were better distributed throughout the mesoporous phase after exsolution. The latter asseveration was confirmed through EDS analyses (Fig. 4c and Fig. 5c) where R-$LaNiO_3$-B sample presented Ni nanoparticles more agglomerated than the ones in R-$LaNiO_3$-S(1.00 g). Therefore, the creation of porosity within the pristine perovskite structure was successful in producing small Ni nanoparticles well distributed on the final catalyst.

NH_3 conversion at different temperatures (Fig. 7a) clearly demonstrates that R-$LaNiO_3$-S(1.00 g) displayed the best catalytic performance of all synthesized perovskites. Even if catalytic tests were carried out at high GHSV (i.e. 30 000 mL/g_{cata}.h), R-$LaNiO_3$-S(1.00 g) reached 89 % of conversion at 550 °C which is 1.35 higher than the conversion accomplished by the R-$LaNiO_3$-B (i.e. 66 %). After assessing the rest of R-$LaNiO_3$-S perovskites, it is possible to observe a trend between specific surface area, Ni dispersion and NH_3 conversion. As the SBA-15 content increased during $LaNiO_3$ preparation, the different perovskites developed a greater specific surface area with small mesopores.

This larger available area allowed a greater dispersion of metallic Ni during the reduction processes under hydrogen, which later translated into a greater number of active sites to achieve better catalytic activity during NH_3 decomposition. This effect of improved Ni dispersion yielded also greater results in terms of H_2 formation rate (Fig. 7b). Precisely, R-$LaNiO_3$-S(1.00 g) achieved 29 mmolH_2/g_{cata}.min while R-$LaNiO_3$-B yielded around 16 mmolH_2/g_{cata}.min (i.e. with 4 times the metallic surface area it was possible to double H_2 productivity). These results demonstrate that the sophisticated synthesis procedure we propose to prepare the investigated catalysts allows reaching very high dispersion of Ni nanoparticles on the exsolved $LaNiO_3$ with correspondingly the achievement of excellent catalytic performance towards NH_3 decomposition and H_2 production.

A lower GHSV = 6 000 mL/g_{cata}.h was also tested in NH_3 decomposition with the reference R-$LaNiO_3$-B perovskite and the best perovskite found in the previous tests, i.e. R-$LaNiO_3$-S(1.00 g). Under these

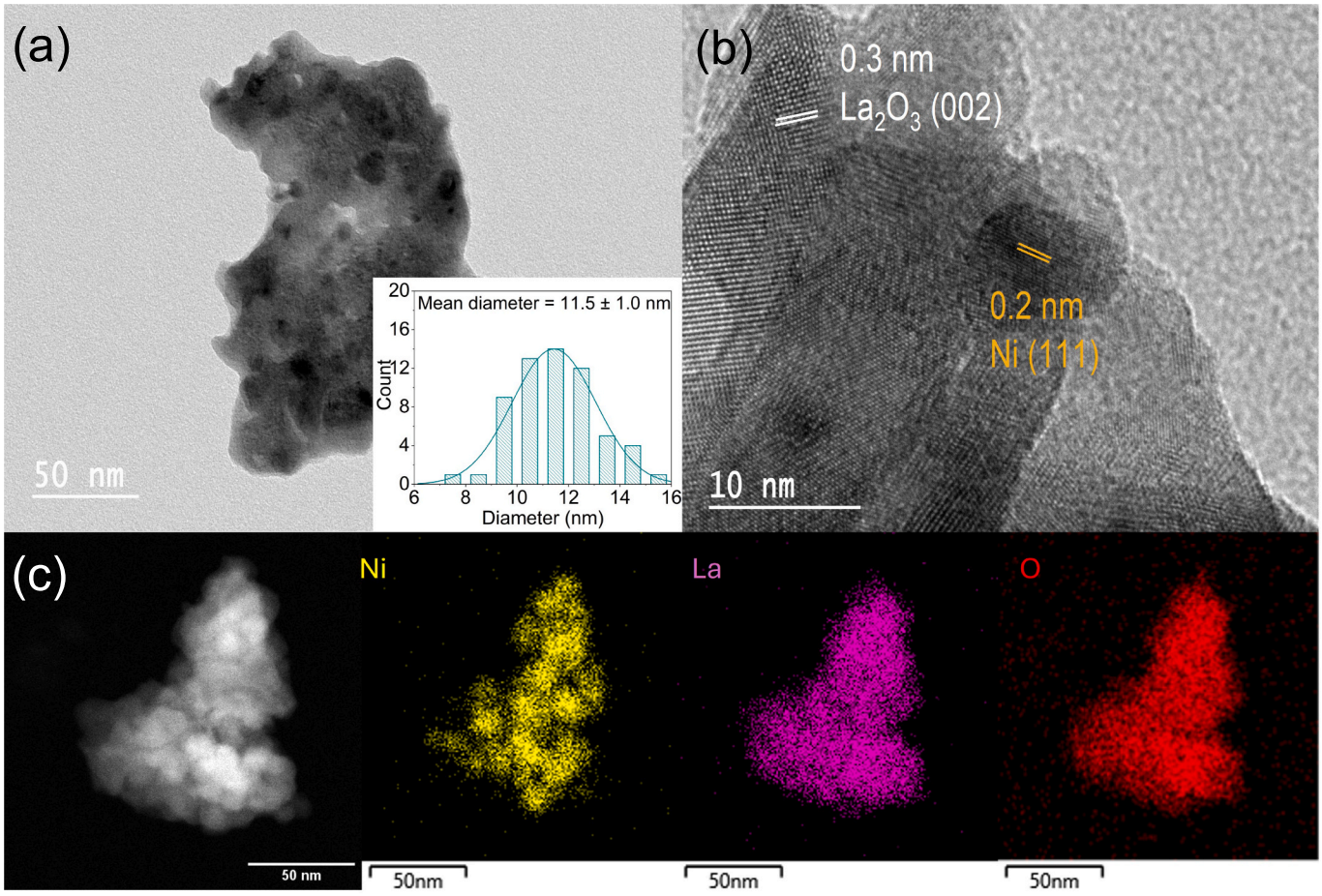

Fig. 5. A) tem image of r-lanio$_3$-B with histogram for Ni nanoparticle size distribution; b) HRTEM of R-$LaNiO_3$-B and c) HADDF-STEM image with EDS elemental mapping from R-$LaNiO_3$-B.

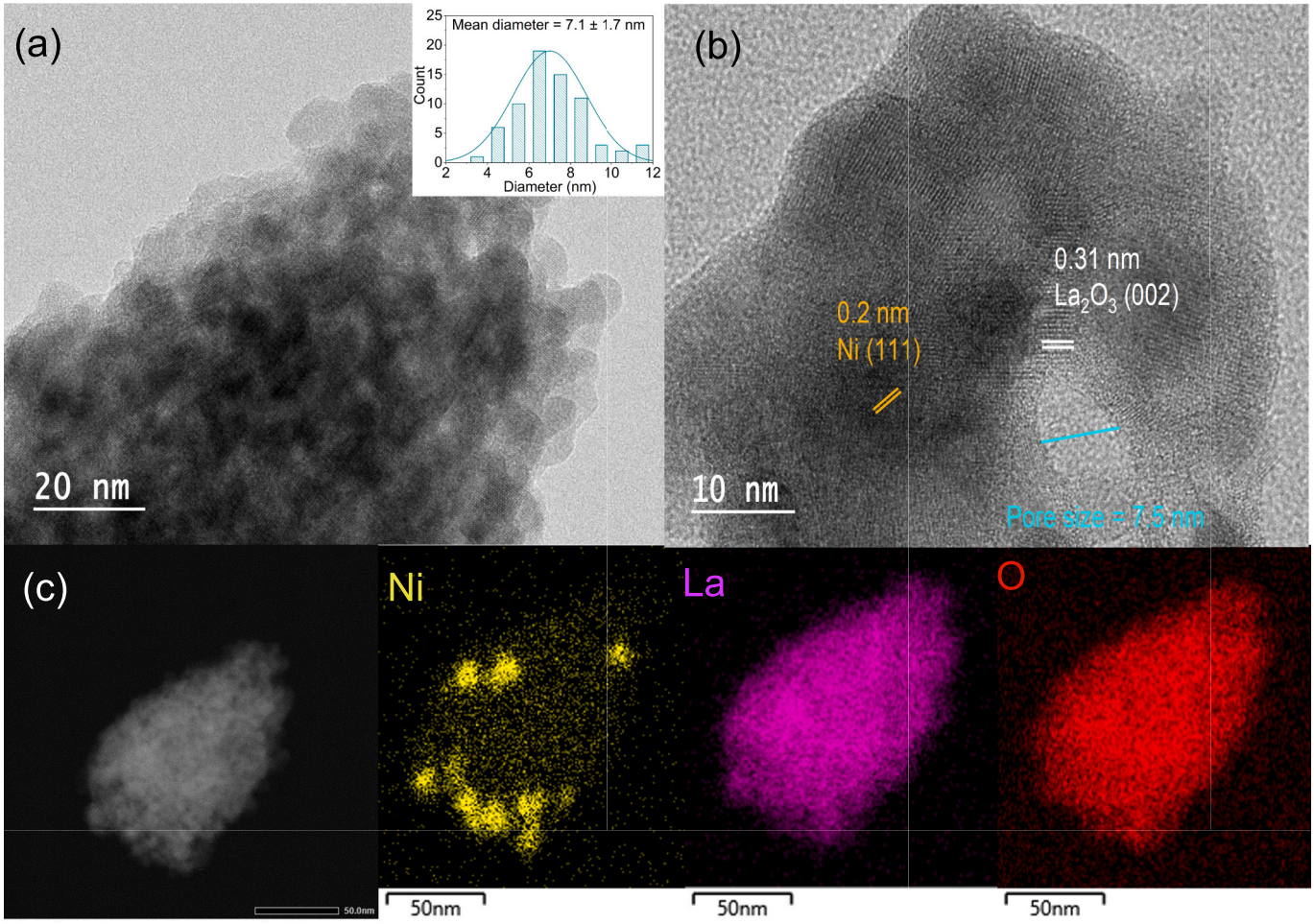

Fig. 6. A) tem image of r-lanio$_3$-S(1.00 g) with histogram for Ni nanoparticle size distribution; b) HRTEM of R-LaNiO$_3$-S(1.00 g) and c) HADDF-STEM image with EDS elemental mapping from R-LaNiO$_3$-S(1.00 g).

conditions, R-LaNiO$_3$-S(1.00 g) totally converts NH_3 into H_2 at 550 °C while R-LaNiO$_3$-B still needs to reach 600 °C to achieve a complete conversion (Fig. 7c). These results again highlight the exceptional efficiency of our Ni-exsolved high specific surface area perovskite. Activation energy (Fig. S7) was also estimated for all samples at GHSV = 30 000 mL/g$_{cata}$.h considering conversions below 20 %. In the case of R-LaNiO$_3$-B, an activation energy of 76 kJ/mol which corresponds to values reported elsewhere [22,23].

As regards R-LaNiO$_3$-S catalysts, activation energies are amid 74 and 65 kJ/mol being R-LaNiO$_3$-S(1.00 g) the sample that displays the lowest activation energy. In addition, these values are even lower than those reported by other authors with doped LaNiO$_3$ [22,23]. Therefore, these results demonstrate that a better Ni dispersion allows reducing the energy barriers required to achieve NH_3 cracking.

Stability tests were conducted at 550 °C with a GHSV = 30 000 mL/g$_{cata}$.h for 72 h. Fig. 7d shows that catalysts keep their catalytic activity throughout all the catalytic test even the bulk perovskite. The maximum catalytic activity is attained after few minutes the reactor reached the targeted temperature. To understand better how these catalysts remained active for a long period of time post-characterization tests were performed (Fig. 8). N_2 physisorption isotherms of R-LaNiO$_3$-S samples kept a high surface area along with small mesopores as before the reaction (Fig. 8a). Specific surface areas and pore volumes (Table 4) are similar to those values before stability tests. In addition, diffractograms on Fig. 8b do not show evidence that catalysts suffered any structure degradation. Hence, there is no evidence of sintering during catalytic tests. The mesoporosity of catalysts remained intact and, as consequence, Ni nanoparticles did not agglomerate which was also confirmed by Ni dispersion estimated through H_2 chemisorption (Table 4).

Catalysts' integrity after stability tests is explained by the embedding of Ni nanoparticles inside La_2O_3 matrix. As a result of the exsolution process, Ni^{3+} (i.e. Ni in the LaNiO3 lattice) was reduced to its metallic state but at the same time the nanoparticles that came out towards the surface were embedded inside La_2O_3 structure [34–36]. This phenomenon prevents Ni sintering at high temperatures which makes it possible to maintain the integrity of catalysts during long run tests.

These outstanding results confirm that the catalytic performance of LaNiO$_3$ can be boosted not only by adding basic promoters or by increasing the exsolution temperature (i.e. reduction treatment) [21–23], but also through the development of sophisticated procedure for the synthesis of the catalysts, maximizing the number of active sites thanks to the achievement of a better dispersion of Ni nanoparticles thanks to its exsolution from mesoporous pristine perovskites.

Table 5 compares the catalytic results obtained by our high specific surface area Ni-exsolved mesoporous LaNiO$_3$ with others published by different authors. Our mesoporous catalysts obtained after Ni exsolution from LaNiO$_3$ shows better conversions and H_2 formation rates than similar catalysts, even better than those of some doped with basic cations such as Ce or Sr. Hence, our work demonstrates that an improvement in LaNiO$_3$ porosity can help to achieve excellent catalytic performances without the need of adding doping agents. When our R-LaNiO$_3$-S are compared with other Ni supported catalysts, the benefits of our Ni-exsolved mesoporous R-LaNiO$_3$-S clearly appear.

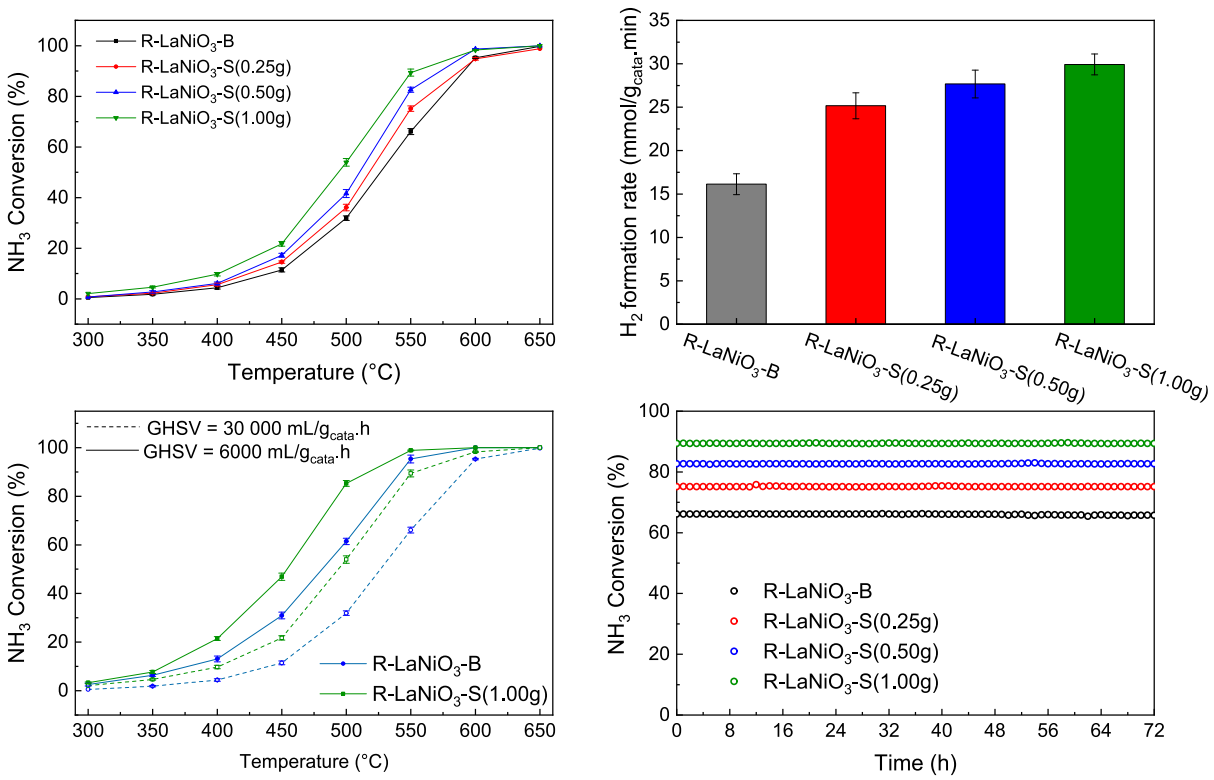

Fig. 7. A) conversions reached by reduced lanio$_3$ at 30 000 mL/g_{cata}.h; b) H_2 formation rate yielded by reduced $LaNiO_3$ at 550 °C and 30 000 mL/g_{cata}.h; c) catalytic performance of R-$LaNiO_3$-B and R-$LaNiO_3$-S(1.00 g) at different GHSV; d) Stability test at 550 °C and a GHSV = 30 000 mL/g_{cata}.h.

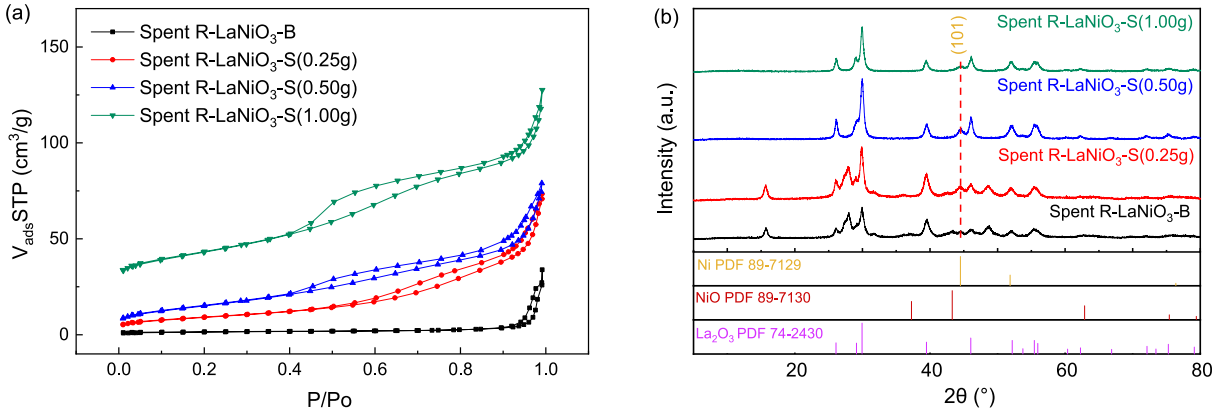

Fig. 8. Post-characterizations analyses: a) N_2 physisorption isotherms after stability tests; b) X-Ray diffractograms of tested catalysts.

Table 4
Textural properties and Ni crystallite size of spent catalysts.

Samples	Textural properties[a]			Ni crystallite size (nm)[b]	Ni dispersion (%)c
	Specific surface area (m^2/g)	**Pore Volume (cm^3/g)**	**Pore diameter (nm)**		
Spent R-$LaNiO_3$-B	4	0.01	45	24.2	0.62
Spent R-$LaNiO_3$-S(0.25 g)	32	0.07	7	23.1	0.82
Spent R-$LaNiO_3$-S(0.50 g)	54	0.08	5	19.2	1.68
Spent R-$LaNiO_3$-S(1.00 g)	132	0.15	4	17.2	2.85

[a] BET and BJH methods; [b]Sherrer equation; [c]H_2 chemisorption

For instance, Wu *et al.*, [39] required 40 wt% of Ni on a mixture of La_2O_3 and MgO in order to reach a conversion ~ 10 % lower than the one achieved by R-$LaNiO_3$-S(1.00 g). The same can be observed in the case of Ni5Co5/SiO_2 catalyst where the addition of Co was not enough to reach similar conversion at 550 °C. Recent examples in literature show different approaches to synthesize high performing catalysts. For instance, Martín *et al.*, [44] deposited Ni nanoparticles on a TiC/SiC matrix. A calcination pretreatment under air atmosphere transformed TiC to TiO_2 which improved metal-support interaction reaching 90 % of NH_3 conversion under a diluted ammonia flow (5 %NH_3/Ar) at 500 °C

Table 5
Comparison of synthesized $LaNiO_3$ catalytic performance with other Ni catalysts.

Catalyst	Ni (wt %)	GHSV ($mL/g_{cata}.h$)	T (°C)	NH_3 Conv. (%)	H_2 rate ($mmol/g_{cata}.min$)	Ref.
R-$LaNiO_3$-B	25.5	30 000	550	66.1	16.1	This work
R-$LaNiO_3$-B	25.5	6000	550	95.3	6.4	This work
R-$LaNiO_3$-S (1.00 g)	**25.2**	**30 000**	**550**	**89.4**	**29.9**	**This work**
R-$LaNiO_3$-S (1.00 g)	**25.2**	**6000**	**550**	**99**	**6.6**	**This work**
$LaCeNiO_3$	––	6000	550	98	6.7	[21]
$LaCeCoO_3$	––	6000	550	92	6.2	[21]
$La_{0.5}Sr_{0.5}NiO_3$-δ-600H_2	25.6	30 000	550	87.7	29.4	[23]
$SrNiO_3$-δ-600H_2	28.6	30 000	550	48.9	16.4	[23]
Ni5Co5/SiO_2	23.4	30 000	550	76.8	25.7	[39]
40Ni/5MgLa	40	30 000	550	82.0	27.1	[40]
Ni1/C-LDHs-ST	23.6	30 000	550	53.0	16.3	[41]
Ni/La_2O_3	40	6000	550	78.9	4.8	[42]
Ni/SBA-15	23.4	30 000	550	89	29.8	[43]
5Ni/TiCSiC-700	5.0	60 000 (stream 5 % NH_3/Ar)	500	92	61.3	[44]
Ce0.2-Co1.5Fe1.5 LDOs	––	30 000	550	80	19.4	[45]
Ni-DML-160	23	12 000	550	89	––	[46]

[44]. Other recent examples reported in literature employed other materials such as a CeO_2-conjugated cobalt ferrite heterostructure or Ni exsolved from a two-dimensional MWW-zeolite that attained high conversion values of 80 % and 89 % at 550 °C respectively [45,46]. In the case of Kim *et al.*, [46] a zeolite with higher surface area yielded metallic Ni with higher dispersion which derived in higher NH_3 conversions [46]. Thereby, those results also confirm what was found in this work with Ni exsolved from modified perovskites.

Therefore, our approach should be considered when preparing $LaNiO_3$ perovskites rather than conventional preparation procedures as our synthesis protocol allows drastically increasing the specific surface area and therefore the catalytic performance. By improving its specific surface area and Ni dispersion, it could be possible later to add basic promoters to boost even more the performance of this material in the production of H_2 via NH_3 decomposition.

4. Conclusions

A yet never explored combination of the citric acid complex method, the use of a hard template (i.e. mesoporous SBA-15) and Ni exsolution through H_2 heating treatment, allowed producing a high specific surface area mesoporous Ni-exsolved $LaNiO_3$ that is particularly active in NH_3 decomposition. Characterization techniques demonstrated that $LaNiO_3$ was formed over the SBA-15 surface without any interference from the latter during the formation of the perovskite. Moreover, the washing with NaOH only dissolved SBA-15 while the $LaNiO_3$ was conserved with a high specific surface area ~200 m^2/g.

XRD and XPS analyses demonstrated that Ni nanoparticles were formed during the exsolution reduction stage under H_2-containing atmosphere. These nanoparticles were better dispersed over the Ni-exsolved perovskite surface when higher amounts of SBA-15 were used in the preparation of the pristine mesoporous $LaNiO_3$. Precisely, the higher the amount of mesoporous hard template used, the more space La and Ni had to better distribute over the SBA-15 surface. This in turn drove to higher specific surface areas which at the end yielded greater Ni dispersions.

Catalytic tests results showed that a better Ni dispersion translated in higher NH_3 conversion with greater H_2 formation rates. Our high specific surface area exsolved mesoporous $LaNiO_3$ was not only very active in the reaction but also stable at the long-term as keeping a conversion around 89 % for 72 h at 550 °C under a GHSV of 30 000 $mL/g_{cata}.h$. A comparison amid our home-made catalysts and the perovskites doped with different cations (i.e. Sr, Ce or even Co) reported in the literature revealed that our Ni-exsolved $LaNiO_3$ with better Ni dispersions are much more active than doped $LaNiO_3$ which in most of the cases present low specific surface areas (i.e. < 20 m^2/g) with low Ni dispersions.

Hence, the development of mesoporous $LaNiO_3$ allows boosting Ni dispersion during the Ni exsolution stage yielding an outstanding catalyst with unprecedented performance for H_2 production through NH_3 decomposition.

Author contributions

The manuscript was written through contributions of all authors. All authors have given approval to the final version of the manuscript. †These authors contributed equally in the conception of the idea and the investigation carried out. ‡This author gave supporting assistance in the development of the research.

Funding Sources

This work was funded by the Synfonhy-UCLouvain project which is co-funded by the European Union and Region Wallonne in Belgium.

CRediT authorship contribution statement

Sebastian Gamez: Writing – original draft, Validation, Methodology, Investigation, Formal analysis, Conceptualization. **Ferdaous Ben Romdhane:** Validation, Formal analysis. **Josefine Schnee:** Writing – review & editing, Validation, Formal analysis. **Eric M. Gaigneaux:** Writing – review & editing, Validation, Resources, Project administration.

Declaration of competing interest

The authors declare that they have no known competing financial interests or personal relationships that could have appeared to influence the work reported in this paper.

Acknowledgment

The authors thank the Fédération Wallonie Bruxelles through the Synfonhy-UCLouvain project for the funding of the present research work.

Appendix A. Supplementary data

Supplementary data to this article can be found online at https://doi.org/10.1016/j.cej.2025.160377.

Data availability

Data will be made available on request.

References

[1] W. Lubitz, W. Tumas, Hydrogen: An overview, *Chem. Rev.* 107 (10) (2007) 3900–3903, https://doi.org/10.1021/cr050200z.
[2] G. Nicoletti, N. Arcuri, G. Nicoletti, R.A. Bruno, A technical and environmental comparison between hydrogen and some fossil fuels, *Energy Convers. Manage.* 89 (2015) 205–213, https://doi.org/10.1016/j.enconman.2014.09.057.
[3] J.O. Abe, A.P.I. Popoola, E. Ajenifuja, O.M. Popoola, Hydrogen energy, economy and storage: Review and recommendation, *Int. J. Hydrogen Energy*. 44 (29) (2019) 15072–15086, https://doi.org/10.1016/j.ijhydene.2019.04.068.

[4] A. Züttel, A. Remhof, A. Borgschulte, O. Friedrichs, Hydrogen: The future energy carrier, *Philos Trans A Math Phys Eng Sci*. 360 (2010) 3329–3342, https://doi.org/10.1098/rsta.2010.0113.

[5] M.A. Rosen, Advances in hydrogen production by thermochemical water decomposition: A review, *Energy* 35 (2) (2010) 1068–1076, https://doi.org/10.1016/j.energy.2009.06.018.

[6] A. El Kharbachi, E. M. Dematteis, K. Shinzato, S. C. Stevenson, L. J. Bannenberg, M. Heere, C. Zlotea, P. A Szilágyi, J. P. Bonnet, W. Grochala, D. H. Gregory, T. Ichikawa, M. Baricco, B. C. Hauback, Metal Hydrides and Related Materials. Energy Carriers for Novel Hydrogen and Electrochemical Storage. *J. Phys. Chem. C*. 124 (14), (2020) 7599–7607. 10.1021/acs.jpcc.0c01806.

[7] S. Chatterjee, R.K. Parsapur, K.W. Huang, Limitations of Ammonia as a Hydrogen Energy Carrier for the Transportation Sector, *ACS Energy Lett*. 6 (12) (2021) 4390–4394, https://doi.org/10.1021/acsenergylett.1c02189.

[8] A. Grinberg Dana, O. Elishav, A. Bardow, G.E. Shter, G.S. Grader, Nitrogen-Based Fuels: A Power-to-Fuel-to-Power Analysis, *Angew. Chem. Int. Ed*. 55 (2016) 8798–8805, https://doi.org/10.1002/anie.201510618.

[9] A. Grinberg Dana, G.E. Shter, G.S. Grader, Nitrogen-Based Alternative Fuel: Safety Considerations, *Energy Technol*. 3 (9) (2015) 976–981, https://doi.org/10.1002/ente.201500180.

[10] P. Yuan, L. Chen, C. Liu, Z. Wang, Numerical Studies on Hydrogen Production from Ammonia Thermal Cracking with Catalysts, *Energies*. 16 (13) (2023) 10.3390/en16135196.

[11] X. Duan, G. Qian, Y. Liu, J. Ji, X. Zhou, D. Chen, W. Yuan, Structure sensitivity of ammonia decomposition over Ni catalysts: A computational and experimental study, *Fuel Process. Technol*. 108 (2013) 112–117, https://doi.org/10.1016/j.fuproc.2012.05.030.

[12] C. Chen, K. Wu, H. Ren, C. Zhou, Y. Luo, L. Lin, C. Au, L. Jiang, Ru-Based Catalysts for Ammonia Decomposition: A Mini-Review, *Energy Fuels*. 35 (2021) 11693–11706, https://doi.org/10.1021/acs.energyfuels.1c01261.

[13] F. Hayashi, Y. Toda, Y. Kanie, M. Kitano, Y. Inoue, T. Yokoyama, M. Hará, H. Hosono, Ammonia decomposition by ruthenium nanoparticles loaded on inorganic electride C12A7:e-, *Chem. Sci*. 4 (8) (2013) 3124–3130, https://doi.org/10.1039/c3sc50794g.

[14] C. Huang, Y. Yu, J. Yang, Y. Yan, D. Wang, F. Hu, X. Wang, R. Zhang, G. Feng, Ru/La_2O_3 catalyst for ammonia decomposition to hydrogen, *Appl. Surf. Sci*. 476 (2019) 928–936, https://doi.org/10.1016/j.apsusc.2019.01.112.

[15] F. Zhiqiang, W. Ziqing, L. Dexing, L. Jianxin, Y. Lingzhi, W. Qin, W. Zhong, Catalytic ammonia decomposition to CO_x-free hydrogen over ruthenium catalyst supported on alkali silicates, *Fuel*. (2022) 326, https://doi.org/10.1016/j.fuel.2022.125094.

[16] T.A. Le, Q.C. Do, Y. Kim, T.W. Kim, H.J. Chae, A review on the recent developments of ruthenium and nickel catalysts for COx-free H_2 generation by ammonia decomposition, *Korean J. Chem. Eng*. 38 (2021) 1087–1103, https://doi.org/10.1007/s11814-021-0767-7.

[17] I. Nakamura, T. Fujitani, Role of metal oxide supports in NH_3 decomposition over Ni catalysts, *Appl. Catal. A*. 524 (2016) 45–49, https://doi.org/10.1016/j.apcata.2016.05.020.

[18] J. Zhang, H. Xu, X. Jin, Q. Ge, W. Li, Characterizations and activities of the nano-sized Ni/Al_2O_3 and Ni/La-Al_2O_3 catalysts for NH3 decomposition, *Appl. Catal., A* 290 (1–2) (2005) 87–96, https://doi.org/10.1016/j.apcata.2005.05.020.

[19] L. Chouhan, S. Ghimire, C. Subrahmanyam, T. Miyasaka, V. Biju, Synthesis, optoelectronic properties and applications of halide perovskites, *Chem. Soc. Rev*. 49 (2020) 2869–2885, https://doi.org/10.1039/c9cs00848a.

[20] K. Wang, C. Han, Z. Shao, J. Qiu, S. Wang, S. Liu, Perovskite Oxide Catalysts for Advanced Oxidation Reactions, *Adv. Funct. Mater*. (2021) 31, https://doi.org/10.1002/adfm.202102089.

[21] S. Podila, H. Driss, A.M. Ali, A.A. Al-Zahrani, M.A. Daous, Influence of Ce substitution in $LaMO_3$ (M = Co/Ni) perovskites for CO_x-free hydrogen production from ammonia decomposition, *Arabian J. Chem*. 15 (1) (2022), https://doi.org/10.1016/j.arabjc.2021.103547.

[22] M. Pinzón, A. Sánchez-Sánchez, A. Romero, A.R. de la Osa, P. Sánchez, Self-combustion Ni and Co-based perovskites as catalyst precursors for ammonia decomposition. Effect of Ce and Mg doping, *Fuel* (2022) 323, https://doi.org/10.1016/j.fuel.2022.124384.

[23] X.Y. Guo, J.H. Wang, Q. Zhang, T.Z. Li, H. Dong, C.J. Jia, C. Li, Y.W. Zhang, Alkaline earth metal promoted hydrogen production from ammonia decomposition over Ni/La_2O_3-based catalysts, *Appl. Catal., b*. 348 (2024) 123844, https://doi.org/10.1016/j.apcatb.2024.123844.

[24] V.L. Zholobenko, A.Y. Khodakov, M. Impéror-Clerc, D. Durand, I. Grillo, Initial stages of SBA-15 synthesis: An overview, Adv. Colloid Interface Sci. 142 (2008) 67–74, https://doi.org/10.1016/j.cis.2008.05.003.

[25] H. Lu, D. Wu, Y. Gu, W. Sun, X. Yang, W. Li, H. Shuai, X. Zhao, A facile mixed complex synthesis method for perovskite oxides toward electrocatalytic oxygen reduction, *Chem. Commun*. 59 (95) (2023) 14149–14152, https://doi.org/10.1039/d3cc04585d.

[26] M. Khettab, S. Omeiri, D. Sellam, M.A. Ladjouzi, M. Trari, Characterization of $LaNiO_3$ prepared by sol-gel: Application to hydrogen evolution under visible light, *Mater. Chem. Phys*. 132 (2–3) (2012) 625–630, https://doi.org/10.1016/j.matchemphys.2011.11.078.

[27] R. Bardestani, G.S. Patience, S. Kaliaguine, Experimental methods in chemical engineering: specific surface area and pore size distribution measurements—BET, BJH, and DFT, *Can. J. Chem. Eng*. 97 (2019) 2781–2791, https://doi.org/10.1002/cjce.23632.

[28] C.G. Sonwane, S.K. Bhatia, Characterization of pore size distributions of mesoporous materials from adsorption isotherms, *J. Phys. Chem. B*. 104 (39) (2000) 9099–9190, https://doi.org/10.1021/jp000907j.

[29] B. Zhao, B. Yan, Z. Jiang, S. Yao, Z. Liu, Q. Wu, R. Ran, S.D. Senanayake, D. Weng, J.G. Chen, High selectivity of CO_2 hydrogenation to CO by controlling the valence state of nickel using perovskite, *Chem. Commun*. 54 (53) (2018) 7354–7357, https://doi.org/10.1039/c8cc03829e.

[30] S. Mickevičius, S. Grebinskij, V. Bondarenka, B. Vengalis, K. Šliužiene, B. A. Orlowski, V. Osinny, W. Drube, Investigation of epitaxial $LaNiO_3$-x thin films by high-energy XPS, *J. Alloys Compd*. 23 (2006) 107–111, https://doi.org/10.1016/j.jallcom.2005.12.038.

[31] T. Maneerung, K. Hidajat, S. Kawi, K-doped $LaNiO_3$ perovskite for high-temperature water-gas shift of reformate gas: Role of potassium on suppressing methanation, *Int. J. Hydrogen Energy*. 42 (15) (2017) 9840–9857, https://doi.org/10.1016/j.ijhydene.2017.01.060.

[32] A.K.R. Police, S. Basavaraju, D. Valluri, S. Machiraju, Photocatalytic activity of Ce-modified SBA-15 for the degradation of isoproturon, *Bull. Mater. Sci*. 38 (1) (2015) 227–234, https://doi.org/10.1007/s12034-015-0840-0.

[33] K. Bai, J. Hao, Y. Yang, A. Qian, The effect of hydrothermal temperature on the properties of SBA-15 materials, *Heliyon*. 6 (8) (2020) e04436, https://doi.org/10.1016/j.heliyon.2020.e04436.

[34] P. Cao, P. Tang, M.F. Bekheet, H. Du, L. Yang, L. Haug, A. Gili, B. Bischoff, A. Gurlo, M. Kunz, R.E. Dunin-Borkowski, S. Penner, M. Heggen, Atomic-Scale Insights into Nickel Exsolution on $LaNiO_3$ Catalysts via In Situ Electron Microscopy, *J. Phys. Chem. C*. 126 (1) (2022) 786–796, https://doi.org/10.1021/acs.jpcc.1c09257.

[35] N. Bonmassar, M.F. Bekheet, L. Schlicker, A. Gili, A. Gurlo, A. Doran, Y. Gao, M. Heggen, J. Bernardi, B. Klötzer, S. Penner, In Situ-Determined Catalytically Active State of $LaNiO_3$ in Methane Dry Reforming, *ACS Catal*. 10 (2) (2020) 1102–1112, https://doi.org/10.1021/acscatal.9b03687.

[36] M. Barreau, D. Salusso, J. Zhang, M. Haevecker, D. Teschner, A. Efimenko, F. Bournel, J.J. Gallet, E. Borfecchia, K. Sobczak, C. Petit, S. Zafeiratos, Uncovering the critical function of lanthanum in CH_4 production from CO_2 using exsolved $LaNiO_3$ perovskite catalysts, *J. Mater. Chem. A*. 12 (2024) 7605–7621, https://doi.org/10.1039/d3ta07391b.

[37] L. Huang, F. Zhang, N. Wang, R. Chen, A.T. Hsu, Nickel-based perovskite catalysts with iron-doping via self-combustion for hydrogen production in auto-thermal reforming of Ethanol, *Int. J. Hydrogen Energy*. 37 (2) (2012) 1272–1279, https://doi.org/10.1016/j.ijhydene.2011.10.005.

[38] C.L. McBean, H. Liu, M.E. Scofield, L. Li, L. Wang, A. Bernstein, S.S. Wong, Generalizable, Electroless, Template-Assisted Synthesis and Electrocatalytic Mechanistic Understanding of Perovskite $LaNiO_3$ Nanorods as Viable, Supportless Oxygen Evolution Reaction Catalysts in Alkaline Media, *ACS Appl. Mater. Interfaces*. 9 (29) (2017) 24634–24648, https://doi.org/10.1021/acsami.7b06855.

[39] Z.W. Wu, X. Li, Y.H. Qin, L. Deng, C.W. Wang, X. Jiang, Ammonia decomposition over SiO2-supported Ni–Co bimetallic catalyst for COx-free hydrogen generation, *Int. J. Hydrogen Energy*. 45 (30) (2020) 15263–15269, https://doi.org/10.1016/j.ijhydene.2020.04.007.

[40] Y. Yu, Y.M. Gan, C. Huang, Z.H. Lu, X. Wang, R. Zhang, G. Feng, Ni/La_2O_3 and Ni/MgO–La_2O_3 catalysts for the decomposition of NH_3 into hydrogen, *Int. J. Hydrogen Energy*. 45 (33) (2020) 16528–16539, https://doi.org/10.1016/j.ijhydene.2020.04.127.

[41] J. Zhao, L. Deng, W. Zheng, S. Xu, Q. Yu, X. Qiu, Nickel-induced structure transformation in hydrocalumite for enhanced ammonia decomposition, International *Int. J. Hydrogen Energy*. 45 (22) (2020) 12244–12255, https://doi.org/10.1016/j.ijhydene.2020.02.201.

[42] H. Muroyama, C. Saburi, T. Matsui, K. Eguchi, Ammonia decomposition over Ni/La_2O_3 catalyst for on-site generation of hydrogen, *Appl. Catal., A*. 443–444 (2012) 119–124, https://doi.org/10.1016/j.apcata.2012.07.031.

[43] H. Liu, H. Wang, J. Shen, Y. Sun, Z. Liu, Preparation, characterization and activities of the nano-sized Ni/SBA-15 catalyst for producing COx-free hydrogen from ammonia, *Appl. Catal., A*. 337 (2) (2008) 138–147, https://doi.org/10.1016/j.apcata.2007.12.006.

[44] C. Martína, P. Sáncheza, A. de Lucas-Consuegraa, M. Pinzóna, A.R. de la Osa, Exploring the preparation of Ni/TiCSiC catalysts for hydrogen production from ammonia, *Chem Eng J*. 502 (2024) 158042, https://doi.org/10.1016/j.cej.2024.158042.

[45] S.U. Lee, T.A. Le, Y. Kim, Y.J. Lee, J.R. Kim, T.W. Kim, K.E. Jeong, H.J. Chae, CeO_2-conjugated CoFe layered double oxides as efficient non-noble metal catalysts for NH_3-decomposition enabling carbon-free hydrogen production, *Chem Eng J*. 500 (2024) 156986, https://doi.org/10.1016/j.cej.2024.156986.

[46] E.J. Kim, Y.W. Kim, Y. Cho, S. Kweon, M.B. Park, C.H. Shin, H.K. Min, K. An, Metallic nickel exsolved from a two-dimensional MWW-type zeolitic nickel silicate: An effective catalyst for ammonia decomposition, *Chem Eng J*. 485 (2024) 4987, https://doi.org/10.1016/j.cej.2024.149871.